Electronic and optical properties of crystalline nitrogen versus black phosphorus: A comparative first-principles study

Alexander N. Rudenko, Swagata Acharya, Ferenc Tasnádi, Dimitar Pashov, Alena V. Ponomareva, Mark van Schilfgaarde, Igor A. Abrikosov, and Mikhail I. Katsnelson

Electronic and optical properties of crystalline nitrogen versus black phosphorus: A comparative first-principles study

Alexander N. Rudenko,[1, *] Swagata Acharya,[1] Ferenc Tasnádi,[2] Dimitar Pashov,[3] Alena V. Ponomareva,[4] Mark van Schilfgaarde,[3, 5] Igor A. Abrikosov,[2] and Mikhail I. Katsnelson[1]

[1]*Radboud University, Institute for Molecules and Materials, 6525AJ Nijmegen, The Netherlands*
[2]*Department of Physics, Chemistry, and Biology (IFM), Linköping University, SE-581 83, Linköping, Sweden*
[3]*King's College London, Theory and Simulation of Condensed Matter, The Strand, WC2R 2LS London, UK*
[4]*Materials Modeling and Development Laboratory, NUST "MISIS", 119049 Moscow, Russia.*
[5]*National Renewable Energy Laboratory, Golden, CO 80401, USA*
(Dated: May 6, 2022)

Crystalline nitrogen (bN) is an allotrope of nitrogen with the black phosphorus (bP) structure recently synthesized at high pressure by two independent research groups [Sci. Adv. 6, eaba9206 (2020), Phys. Rev. Lett. 124, 216001 (2020)]. Here, we present a systematic study of the electronic and optical properties of bN focusing on its comparison with bP. To this end, we use the state-of-the-art quasiparticle self-consistent GW approach with vertex corrections both in the electronic and optical channels. Despite many similarities, the properties of bN are found to be considerably different. Unlike bP, bN exhibits a larger optical gap (2.5 vs. 0.26 eV) making bN transparent in the visible spectral region with highly anisotropic optical response. This difference can be primarily attributed to a considerably reduced dielectric screening in bN, leading to enhancement of the effective Coulomb interaction. Despite relatively strong Coulomb interaction, exciton formation is largely suppressed in both materials. Our analysis of the elastic properties shows exceptionally high stiffness of bN, comparable to that of diamond.

I. INTRODUCTION

Nitrogen is one of the most abundant elements on Earth, occurring in a gaseous or liquid form. Solid nitrogen is by far less common and is mostly known in the form of molecular N_2 crystals which is, for instance, a main component of Pluto [1]. Other forms of nitrogen include polymeric forms [2, 3] and crystals with the highly unusual cubic gauche structure [4, 5] stabilized at high pressure. Another allotrope of nitrogen, the so-called black nitrogen (bN) has been recently synthesized at high pressure by two independent research groups [6, 7]. bN adopts the orhorhombic (A17) crystal structure, identical to that of black phosphrous (bP).

Exotic forms of matter often demonstrate unusual properties, which attract interest from the research community. In high-pressure physics, the most prominent example is metallic hydrogen, an elusive material, expected to exhibit a variety of remarkable properties including high-temperature superconductivity [8] and the ultimate speed of sound [9]. Understanding the properties of previously unknown phases of elemental compounds is of importance for fundamental science as it complements our knowledge of trends running through the periodic table. Next to that, studies of solid nitrogen are relevant in the context of high energy density materials.

Among the group-V materials, bP is a well-known and thoroughly studied material, which was rediscovered several years ago from the perspective of a two-dimensional material [10–12]. Unlike bP, the properties of bN are largely unexplored. Apart from basic spectroscopic characteristics [6, 7], information about their microscopic origin and physical mechanisms behind the observable properties remain unclear. In this work, we perform a systematic first-principles analysis of the electronic, optical, and vibrational properties of bN at the experimental pressure conditions. We start from density functional calculations and use the quasiparticle self-consistent GW method with vertex corrections to accurately describe the optical response. We focus on the comparison with bP and underline mechanisms responsible for the difference between the properties of bN and bP.

The rest of the paper is organized as follows. In Sec. II, we briefly describe theoretical methods and provide computational details. In Secs. III A and III B, we present our results on the electronic structure and optical properties of bN and bP, which are calculated at different levels of theory. We then analyse the Coulomb interaction and screening in these two materials (Sec. III C). Sec. III D is devoted to a comparative analysis of the vibrational characteristics and elastic properties. In Sec. IV, we briefly summarize our results and conclude the paper.

II. COMPUTATIONAL DETAILS

Electronic and optical properties. We study electronic structure and optical properties of bN/bP at three different levels of theory: density functional theory (DFT) within the local density approximation (LDA), quasiparticle self-consistent GW approximation (QSGW) [13, 14], and an extension of QSGW where the random phase approximation (RPA) to the polarizability is extended by adding ladder diagrams (QS$G\widehat{W}$) [15, 16]. The optical
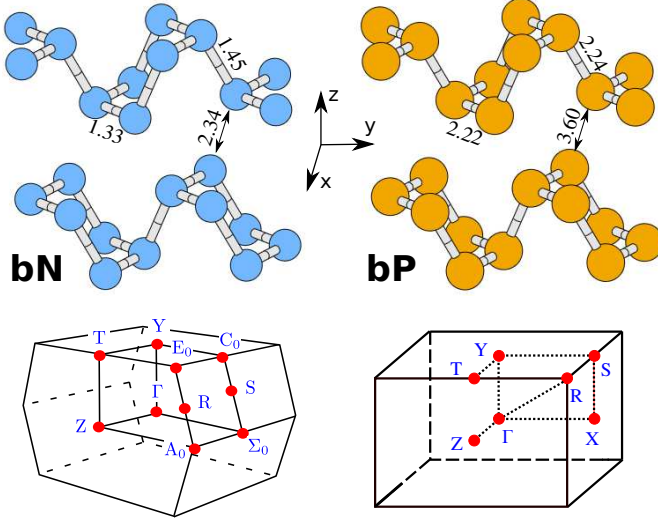
FIG. 1. Top: Schematic crystal structure of bN (left) and bP (right). The numbers correspond to the bond lengths in Å. Bottom: Brillouin zone with high-symmetry points for primitive (left) and conventional (right) unit cells of bN/bP containing 4 and 8 atoms, respectively.
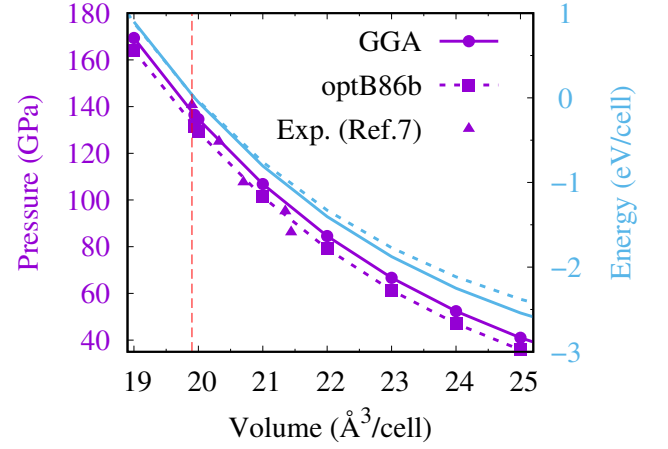

FIG. 2. Pressure and total energy shown as a function of the primitive cell volume calculated for bN with GGA and optB86b functionals. Experimental pressures from Ref. 7 are shown for comparison. Vertical line corresponds to the experimental volume ($V_{\mathrm{exp}} \approx 20$ Å^3) used in this work. Zero total energy corresponds to the energy calculated at V_{exp}.

properties are calculated by incorporating the electron-hole two-particle correlations within a self-consistent ladder-BSE implementation [15, 16] with Tamm-Dancoff approximation [17, 18]. For bP (bN), DFT calculations and energy band calculations with the static quasiparticle QSGW and QS$G\widehat{W}$ self-energy $\Sigma^0(k)$ were performed on a $24{\times}24{\times}12$ ($18{\times}14{\times}6$) **k**-mesh while the dynamical self-energy $\Sigma(\mathbf{k})$ was constructed using a $8{\times}8{\times}4$ ($9{\times}7{\times}3$) **k**-mesh and $\Sigma^0(\mathbf{k})$ extracted from it. For each iteration in the QSGW and QS$G\widehat{W}$ self-consistency cycle, the charge density was made self-consistent. The QSGW and QS$G\widehat{W}$ cycles were iterated until the root-mean-square change in Σ^0 reached 10^{-5} Ry. Thus the calculation was self-consistent in both $\Sigma^0(\mathbf{k})$ and the density. We observe that for bP the QS$G\widehat{W}$ band gap stops changing once 4 valence and 2 conduction bands are included in the two-particle Hamiltonian, while for bN, the convergence was achieved with 12 valence and 12 conduction bands. We use **k**-mesh of $24{\times}24{\times}12$ and $9{\times}14{\times}5$ for computation of the real and imaginary parts of the dielectric response functions for bP and bN, respectively. In both the cases, an energy dependent optical broadening parameter that varies from 10 meV at ω=0 to 1 eV at ω=27.2 eV is used. The **k**-point convergence of the dielectric function is shown in Appendix (Fig. 9). The electronic structure calculations have been performed on a conventional orthorhombic unit cell containing 8 atoms. Experimental lattice parameters were used in all cases.

Coulomb interactions. Coulomb interactions were calculated in the Wannier function (WF) basis using the procedure implemented in VASP [19–23]. For this purpose, we carried out calculations within the projected augmented wave formalism (PAW) [24, 25] using the generalized-gradient approximation (GGA) functional in the Perdew-Burke-Ernzerhof parametrization [26]. A 400 (250) eV energy cutoff for the plane-waves and a convergence threshold of 10^{-8} eV were used for bN (bP). The calculations for both compounds were performed using a primitive cell containing 4 atoms. The Brillouin zone was sampled by a $(6{\times}6{\times}8)$ **k**-point mesh. The WF were calculated considering four WFs per atom (sp-basis) using the scheme of maximal localization [27, 28] using the WANNIER90 package [29]. The screening was considered at the full RPA level [30] taking *all* possible empty states into account within the given plane-wave basis. Specifically, we used 375 (696) bands in total, respectively, for bN (bP). The effective on-site and inter-site Coulomb interaction was calculated by averaging the orbital components of the Coulomb matrix as $U_{\mathrm{eff}}(\mathbf{R}_{ij}) = 1/16 \sum_{mn} U_{mn}(\mathbf{R}_{ij})$, where i and j are the atomic, and m and n are the orbital indices.

Phonon excitations and elastic properties. The vibrational and elastic properties have been calculated with DFT as implemented in VASP [19, 20] using PAW formalism [24, 25]. The exchange correlation energy was approximated by the Perdew-Burke-Ernzerhof GGA functional [26]. A 540 eV energy cutoff and a $(5 \times 5 \times 5)$ **k**-point sampling of the Brillouin zone were used with $(4 \times 4 \times 4)$ sized supercells, which is sufficient to obtain converged phonon dispersions. The phonon calculations have been performed by finite displacement method implemented into PHONOPY [31]. The pressures have been derived from the diagonal elements of the stress tensor calculated for the supercells with optimized atomic positions. The Raman active modes have been derived by factor group analysis of the vibrations [32] at the Γ point. The elastic constants C_{ij} have been calculated using

enthalpy-strain relationships applying $\pm 1, \pm 2\%$ strain to the primitive cell containing 4 atoms. In these calculations, we used a $(12 \times 12 \times 12)$ **k**-point mesh to sample the Brillouin zone. The sound velocities have been derived by solving the Christoffel equation based on the elastic constants. The anisotropic Young modulus $E(\mathbf{n})$ has been calculated as defined in [33] using a (201×51) mesh of the polar and azimuth angles defining the directional normal vector **n**.

Crystal structure. The crystal structures of bN and bP are schematically shown in Fig. 1 along with the Brillouin zones of the primitive and conventional unit cells. The structure consists of puckered layers stacked along the z direction, and corresponds to the A17 phase with space group $Cmca$ (No. 64). For bP, this structure is thermodynamically stable up to $\sim$5 GPa, at which it transforms into a layered rhombohedral (A7) phase [34, 35]. In contrast, bN is unstable under ambient conditions, but can be stabilized at high pressure of 140–150 GPa [6, 7]. Here, we use these conditions and the corresponding experimental lattice parameters to study the properties of bN. With the experimental lattice parameters used in this work, the hydrostatic stress calculated using GGA corresponds to 138 (2.4) GPa for bN (bP).

It should be noted that experimentally it was possible to decompress bN down to 48 and 86 GPa after the synthesis (Refs. 6 and 7, respectively). Figure 2 shows pressure and total energy as a function of the primitive cell volume calculated for bN with (GGA) and without (optB86b [36]) van der Waals interactions taken into account. Both exchange-correlation functionals yield essentially similar behavior, indicating that the van der Waals interactions do not play a significant role in thermodynamics of bN. The pressure vs. volume dependence is in agreement with the experimental data from Ref. 7. For the volumes considered, pressure behaves monotonically spanning a wide range of values, suggesting stability of the A17 structural phase upon decompression down to at least 40 GPa. The dynamical stability of this phase is also confirmed by the absence of imaginary modes in the phonon spectrum of bN above 22 GPa.

III. RESULTS

A. Electronic structure

Figure 3 shows single-particle band structure of bN and bP calculated using DFT (LDA), QSGW, and QS$G\widehat{W}$ methods. Table I summarizes the calculated band gaps. At the DFT level, both bN and bP are metals, showing overlap between the valence and conduction bands, with the negative (inverted) gaps of -0.15 and -0.4 eV, respectively. The single shot GW based on LDA produces positive gap of $\sim$0.1 eV in bP and 0.8 eV in bN. Both QSGW, and QS$G\widehat{W}$ result in the formation of a direct gap at the Γ point. For bP, a gap of $\sim$0.3 eV is found, in agreement with previous GW calculations [37],
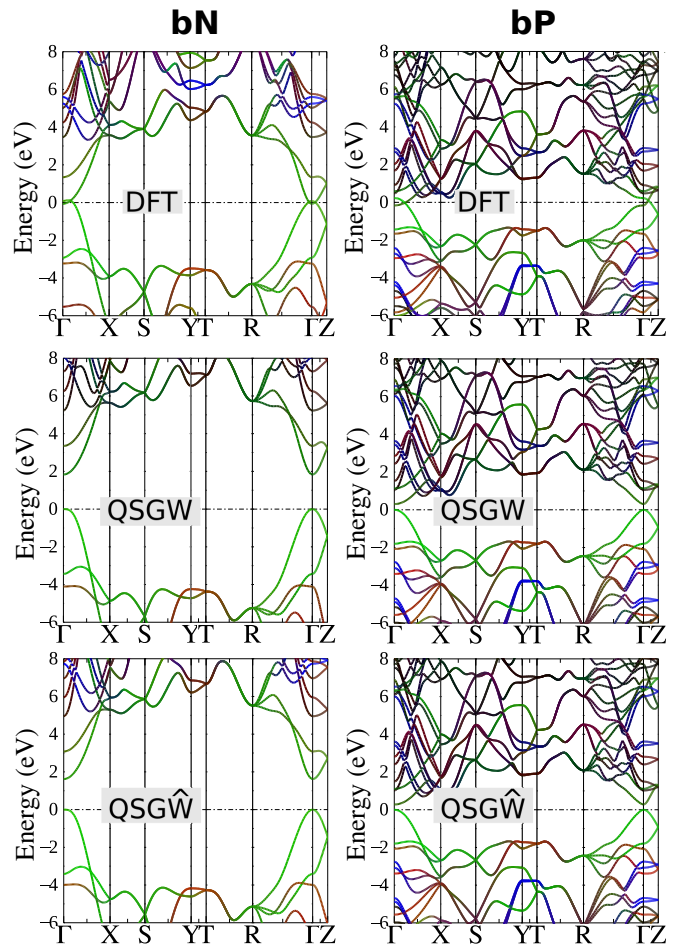

FIG. 3. Single-particle band structure of bN (left) and bP (right) calculated using: DFT (LDA), QSGW, and QS$G\widehat{W}$ approaches (from top to bottom) along high-symmetry directions of the conventional Brillouin zone (Fig. 1). The colors correspond to the contribution of p_x (blue), p_y (red), and p_z (green) orbitals.

as well as with experimental measurements [38–40]. For bN, the gap turns out to be significantly larger, reaching 1.6 eV at QS$G\widehat{W}$, which suggests that screening in bN is smaller than in bP. This can be attributed to the suppression of the Coulomb screening in bN, as will be shown in Sec. III C.

Figure 4 shows density of states (DOS) projected onto

TABLE I. Band gaps (in eV) calculated for bN and bP at different levels of theory. The BSE optical gap from is determined by the energy of the deepest lying bright exciton.

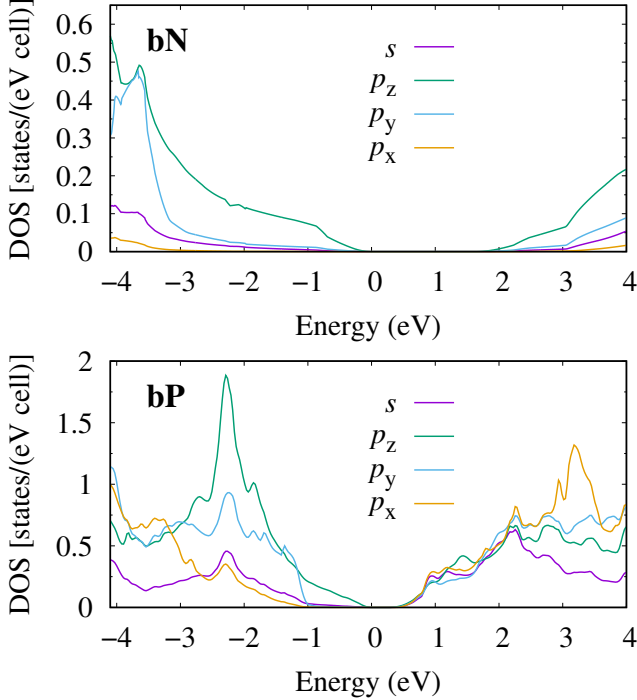|	DFT	QSGW[a]	QS$G\widehat{W}$[a]	RPA@QS$G\widehat{W}$[b]	BSE@QS$G\widehat{W}$[b]
bN	metal	1.88	1.61	3.0	2.50
bP	metal	0.30	0.28	0.28	0.26

[a] Single-particle gap
[b] Optical gap

FIG. 4. Density of states projected onto different orbital states calculated for bN (top) and bP (bottom) using the QS$G\widehat{W}$ approach.

different orbital contributions in bN and bP calculated using QS$G\widehat{W}$. Unlike bP, where the conduction band constitutes a mixture of the s and p states, the conduction band of bN is mainly composed of the p_z states. In contrast, the primary contribution to the valence band edge results from the p_z states in both materials. Overall, sp electronic states of bN are characterized by a smaller density, spanning a larger energy range compared to bP.

Table II summarizes the effective masses calculated for bN and bP using QSGW and QS$G\widehat{W}$ methods. The electron effective masses in the xy direction are similar for bN and bP, being highly anisotropic with the ratio $m_x/m_y \sim 10$. In the direction perpendicular to the layer stacking (z) the effective mass of bN ($m_z \approx 0.5m_e$) is significantly larger than in bP ($m_z \approx 0.1m_e$). These results are consistent between the QSGW and QS$G\widehat{W}$ methods. Larger m_z implies that the states are less dispersed along the k_z direction, indicating a weaker overlap between the wave functions of the interacting layers. This overlap is not favorable energetically as the corresponding interlayer hopping integrals are positive [37]. This means that the band contribution to the interlayer binding is repulsive, and the repulsion is weaker in bN.

The situation with the hole effective masses is qualitatively similar between the materials with one exception. Namely, the hole effective masses calculated along the zigzag (x) direction in bN are anomalously high, resulting in $6.1m_e$ and $12.1m_e$ within QSGW and QS$G\widehat{W}$, respectively, which is an order of magnitude larger compared to

bP. We note that this anomaly is not related to any topological peculiarities of the Fermi surface, as indicated by the absence of the van Hove singularities in the calculated DOS (Fig. 4). Instead, this mass enhancement can be solely attributed to the correlation effects. Unlike all other cases, m_x for holes is considerably different within QSGW and QS$G\widehat{W}$, which indicates an important role of the vertex corrections. We do not exclude that higher order diagrams, not considered here, might be also important for a correct determination of m_x in bN.

B. Optical response

In our calculations, we use a rectangular unit cell, thus the crystal axes x, y, and z correspond to the principal axes. In this situation the dielectric tensor $\varepsilon^{\alpha\beta}$ is diagonal in the absence of magnetic fields. Figure 5 shows imaginary parts of the corresponding frequency-dependent diagonal components $\varepsilon_2^{\alpha\alpha}$ ($\alpha = x, y, z$) calculated at the RPA@QS$G\widehat{W}$ and BSE@QS$G\widehat{W}$ levels for bN and bP. In the relevant spectral region, the strongest absorption is along the y-direction (armchair) for both bN and bP. This can be attributed to low effective masses in the corresponding direction (see Table II), which is also reflected in DOS (Fig. 4). On the other hand, large effective masses along x and z suppress the dipole transition matrix elements, which determine the optical absorption. It should be noted that the corresponding matrix elements are not symmetry-forbidden at the onset of $\varepsilon_2(\omega)$.

For bP, the optical gap obtained within RPA coincides with the single-particle band gap (see Table I), as expected. The vertex corrections applied at the BSE level slightly reduce the gap, yielding 0.26 eV of optical gap (20 meV exciton binding energy), being consistent with previous theoretical studies, as well as with recent experiments [40]. There are no new features appear in the spectrum after the inclusion of the vertex corrections, demonstrating that their effect is not significant, in agreement with earlier findings [41].

The situation with bN is less trivial. Already the RPA calculations show that the optical gap (3.0 eV) is dramatically different from the single-particle gap (1.6 eV).

TABLE II. Electron and hole effective masses (in units of free electron mass) calculated for bN and bP along three crystallographic directions using QSGW and QS$G\widehat{W}$ approximations.

	bN			bP		
	m_x	m_y	m_z	m_x	m_y	m_z
Electrons[a]	1.19	0.14	0.52	1.11	0.09	0.12
Electrons[b]	1.25	0.14	0.54	1.11	0.09	0.12
Holes[a]	6.11	0.23	0.51	0.67	0.08	0.28
Holes[b]	12.14	0.23	0.52	0.67	0.08	0.28

[a] QSGW approximation
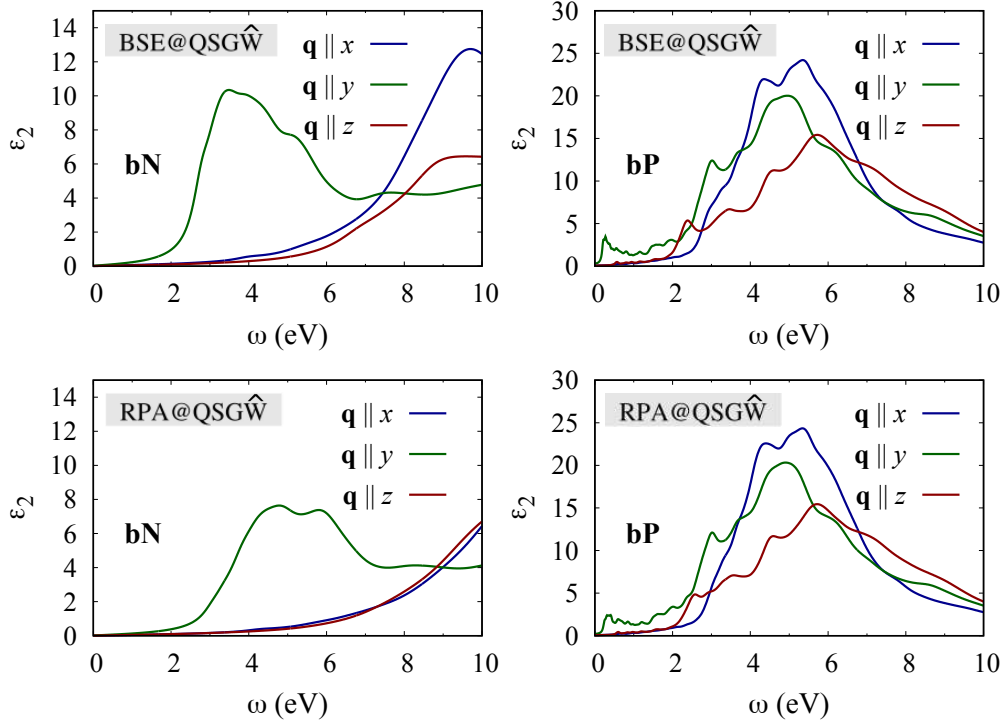[b] QS$G\widehat{W}$ approximation

FIG. 5. Imaginary part of the diagonal components of the dielectric tensor calculated as a function of frequency using RPA@QS$G\widehat{W}$ (top) and BSE@QS$G\widehat{W}$ (bottom) for bN (left) and bP (right).
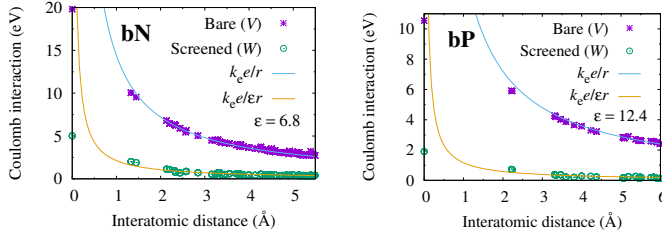

FIG. 6. Effective Coulomb interaction as a function of the interatomic distance in bN and bP. Violet and cyan dots correspond to the bare (V) and screened (W) interactions, respectively. Lines correspond to the classical $V(r) = k_e e/r$ and screened classical $W(r) = V(r)/\varepsilon$ Coulomb interaction, where ε is the effective screening constant.

TABLE III. Effective onsite and intersite Coulomb interaction for bN and bP without (V) and with (W) screening effects considered at the full RPA level. 1NN and 2NN denote nearest- and next-nearest-neighbor, respectively. d is the distance between the corresponding atoms.

	bN			bP		
	Onsite	1NN	2NN	Onsite	1NN	2NN
d (Å)	-	1.33	1.45	-	2.22	2.24
V (eV)	19.8	10.0	9.5	10.5	5.9	5.9
W (eV)	5.0	2.0	1.9	1.9	0.7	0.7

This can be ascribed to the orbital composition of the valence and conduction bands in bN (see projected DOS in Fig. 4). In contrast to bP, the s states do not contribute to the valence and conduction band edges, which are predominantly composed of the p_z states. This means that the dipole transitions between the band edges are symmetry forbidden, resulting in a vanishing optical absorption at the single-particle gap energies. At higher energies, as different angular momenta mix, the dipole transitions become allowed, ensuring finite absorption at 3.0 eV. The presence of vertex corrections further reduces this value by ∼0.5 eV, yielding the optical gap of 2.5 eV. Therefore, our BSE@QS$G\widehat{W}$ calculations demonstrate that pristine

bN can absorb the blue part of the visible spectrum. Additionally, we find four dark e-h eigenvalues at lower energies (1.35, 1.87, 1.92 and two degenerate eigenvalues at 2 eV) compared to the optical gap edge. Although these dark excitons are not important for optical absorption, they might be important for exciton dynamics and photoluminescence. Nevertheless, for both bP and bN, mostly the valence band maximum and conduction band bottom contribute to the low energy optical absorption. The excitons in these materials are Wannier-Mott type, in contrast with the Frenkel excitons in compounds like CrX_3 [42] where all Cr-d bands participate in the low energy optical absorption.

C. Coulomb interaction and screening

To explain the huge difference between the band gaps in bN and bP, we analyze the Coulomb interactions in both materials. Figure 6 shows the effective Coulomb interaction calculated for bN and bP, where both bare (V) and fully screened (W) values are plotted as a function of the interatomic distance. The onsite interactions as well as intersite interactions up to the second nearest-neighbor are also summarized in Table III. The bare onsite interaction in bN (19.9 eV) is larger by a factor of $\sim$1.9 compared to that in bP (10.5 eV). This can be understood in terms of the difference in orbital localization in these two materials. Indeed, an average quadratic spread of the corresponding sp Wannier orbitals obtained within the maximum-localization procedure is found to be 0.5 and 2.7 Å^2 for bN and bP, respectively. The ratio of the *screened* onsite interactions is only slightly larger ($W^{\mathrm{bN}}/W^{\mathrm{bP}} \sim 2.6$), indicating that the local screening effects are comparable in bN and bP. The situation with the interatomic (nonlocal) interactions is different. Interestingly, already from the first nearest-neighbor, the bare interaction is well-described by the classical Coulomb potential $V(r) = k_e e/r$ for both bN and bP, where $k_e = 1/4\pi\varepsilon_0$ is the Coulomb constant. The screened intersite interaction can be reasonably-well fitted by the potential $W(r) = V(r)/\varepsilon$ with ε being an effective screening constant. The values of ε are estimated as 6.8 and 12.4 for bN and bP, respectively, indicating that the screening in bP is considerably more efficient. At the same time, strong screening can be related to large DOS (see Fig. 4) in a wide region around the band gap, resulting in an enhancement of the optical spectral weight at all relevant frequencies. Overall, the Coulomb interactions in bN are considerably larger compared to bP. At the level of the perturbation theory, this means that many-body corrections should lead to a larger self-energy, which explains a wider band gap observed in bN. We note that the obtained screened interactions might be somewhat overscreened and, therefore, underestimated because the calculations are based on the DFT band structure without many-body corrections.

To gain more insight into the dielectric screening in bN and bP, in Table IV we provide the ion-clamped static dielectric function ε_{ii}^∞ $(ii = xx, yy, zz)$ extracted from the BSE-corrected optics and resolved in three crystallographic directions. In agreement with the results presented in Fig. 6, one can see that the screening in bP

TABLE IV. Diagonal components of the ion-clamped static dielectric tensor ε_{ii}^∞ $(ii = xx, yy, zz)$ derived from the BSE@QS$G\widehat{W}$ calculations.

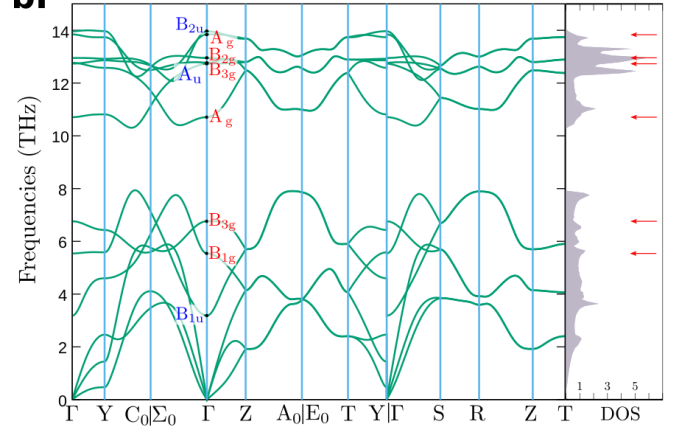|	xx	yy	zz
bN	7.1	9.5	6.0
bP	12.9	16.1	10.4
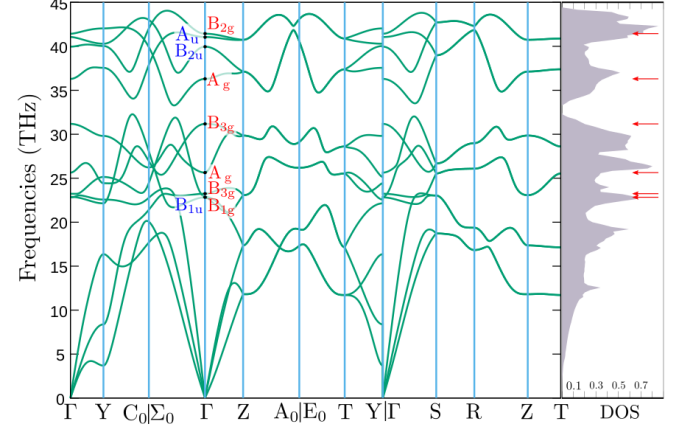
FIG. 7. Phonon dispersion and phonon density of states calculated along high-symmetry direction of the primitive Brillouin zone (Fig. 1) for bN and bP. The labels at the Γ points indicate symmetries of the corresponding optical modes according to irreducible representations of the D_{2h} point group. Red arrows denote frequencies of the Raman-active modes.

is considerable larger than in bN, in all three directions. Next to that, the screening is highly anisotropic in both materials, and is highest in the armchair (y) direction. This observation is consistent with the fact that the optical edge is mainly determined by the yy-component of the dielectric function (Fig. 5).

D. Vibrational and elastic properties

Figure 7 shows the calculated phonon dispersions and density of states (DOS). Although the dispersions show a large degree of similarity between bN and bP, one observes much higher vibrational frequencies in bN. While the largest optical frequency in bP is found around 14 THz, the corresponding value reaches 44 THz in bN, i.e. more than three times higher. This difference cannot be explained by the mass difference between N and P atoms, $\omega^{\mathrm{bP}}/\omega^{\mathrm{bN}} \neq \sqrt{m_N/m_P} \approx 1.5$. Apparently, it
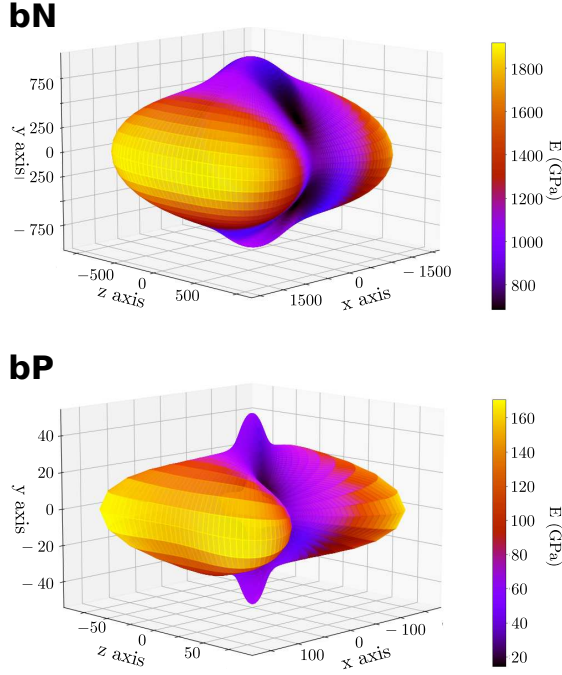
bN

bP

FIG. 8. Orientation dependence of the Young's modulus $E(\mathbf{n})$ in bN and bP.

is attributed to stronger interatomic interactions in bN, which is exaggerated by external pressure.

In systems with D_{2h} point group symmetry like bN and bP, the zone center optical phonons can be classified according to irreducible representations of the point group as follows

$$\Gamma_{D_{2h}} = 2A_g + B_{1g} + B_{2g} + 2B_{3g} + A_u + 2B_{1u} + 2B_{2u} + B_{3u}.$$

The corresponding mode symmetries are indicated in Fig. 7 by blue and red labels. The modes with *gerade* parity (red) can be characterized as Raman-active, whose frequencies listed in Table V. Our results for both bN and bP agree well with those reported earlier in Refs. 7, 43, and 44.

The low-frequency phonons shown in Fig. 7 are characterized by one longitudinal and two transverse branches. In order to gain more insight into the behavior at long wavelengths, we have calculated the sound velocities for different crystallographic directions and polarization, with the results summarized in Table VI. As expected, the sound velocities are highly anisotropic in both ma-

TABLE V. Raman active phonon modes (in THz) calculated for bN and bP shown in accordance with irreducible representations of the D_{2h} point group.

	B_{1g}	B_{3g}	A_g	B_{3g}	A_g	B_{2g}
bN	22.9	23.2	25.6	31.2	36.3	41.4
bP	5.6	6.8	10.7	12.8	13.9	13.0

TABLE VI. Sound velocities (in km/s) calculated for different crystallographic directions for longitudinal (L) and two transverse components (T_1 and T_2) of the polarization in bN and bP. Θ_D is the Debye temperature in K.

	bN			bP		
	L	T_1	T_2	L	T_1	T_2
v_x	21.1	9.3	12.6	8.4	2.5	4.8
v_y	14.9	9.3	7.4	4.4	2.5	1.3
v_z	13.7	12.6	7.4	4.1	4.8	1.3
Θ_D		1840			314	

terials. It is worth noting that the anisotropy of elastic-related properties is considerably smaller in bN, which is likely related to the effect of pressure. The highest velocities are found for phonons propagating in the zigzag (x) directions with the longitudinal polarization. In this case, we obtain 21.1 km/s for bN, which is larger that the sound velocity in diamond, and only 1.7 times smaller than the ultimate speed of sound [9]. In bP, the resulting values are 2–3 times smaller compared to bN.

In Fig. 8, we show a comparison between the orientation-dependent Young's modulus $E(\mathbf{n})$ in bN and bP. The overall shape of the curve is similar for the two materials, with bN being less anisotropic than bP. Remarkably, bN is characterized by exceptionally high Young's modulus, reaching 1916 GPa in the zigzag (x) direction, an order of magnitude larger than in bP. The least stiff direction corresponds to the direction of the layer stacking (z). Even in this case, the Young's modulus of compressed bN is found to be around 686 GPa vs. 15 GPa in bP. The polycrystalline Young modulus calculated using the Hill's averaging is found to be 1077 (57) GPa in bN (bP). The corresponding shear modulus amounts to 451 (23) GPa. The average Poisson's ratio is comparable in both materials, taking the value of 0.20.

IV. CONCLUSION

Motivated by the recent synthesis of crystalline nitrogen with the orthorhombic A17 crystal structure, we have systematically studied electronic, optical, vibrational, and elastic properties of this compound at the experimental pressure conditions. To this end, we used density functional theory combined with the state-of-the-art quasiparticle self-consistent GW approach with vertex corrections included both in the electronic and optical channels. Our analysis is focused on the comparison with black phosphorus, in order to elucidate mechanisms behind the difference between the two materials.

From the electronic and optical points of view, bN is characterized by a considerably larger optical gap (2.5 vs. 0.26 eV), which ensures transparency in the visible spectral region. This difference can be ascribed to the large

Coulomb interactions between the p orbitals of nitrogen, resulting from a reduced dielectric screening. Despite the fact that the role of vertex corrections is significant in this case, it does not lead to the emergence of the excitonic peaks inside the gap, similar to bP. Unlike bP, the hole effective masses along the zigzag direction in bN are anomalously high ($m_x \sim 10m_e$), giving rise to highly anisotropic electronic structure at the valence band edge.

The spectrum of phonon excitations in bN spans a wider energy range compared to bP, which is not surprising. However, this difference cannot be solely explained by the atomic mass difference, and indicates much stronger interatomic interactions in bN. This is further demonstrated by the exceptionally high stiffness of bN, which is comparable to that of diamond. Furthermore, bN is characterized by very high sound velocities, which are close to their ultimate limit.

Appendix: K-point convergence of the optical absorption spectrum in bN

Fig. 9 shows the convergence of the dielectric function $\varepsilon_2^{yy}(\omega)$ in bN with respect to the **k**-point mesh calculated within RPA@QS$G\widehat{W}$ and BSE@QS$G\widehat{W}$. Additionally, the convergence of the deepest lying dark e-h eigenvalue is also shown.

[1] S. A. Stern, F. Bagenal, K. Ennico, G. R. Gladstone, W. M. Grundy, W. B. McKinnon, J. M. Moore, C. B. Olkin, J. R. Spencer, H. A. Weaver, *et al.*, The pluto system: Initial results from its exploration by new horizons, Science **350**, aad1815 (2015).

[2] Y. Ma, A. R. Oganov, Z. Li, Y. Xie, and J. Kotakoski, Novel high pressure structures of polymeric nitrogen, Phys. Rev. Lett. **102**, 065501 (2009).

[3] D. Laniel, G. Geneste, G. Weck, M. Mezouar, and P. Loubeyre, Hexagonal Layered Polymeric Nitrogen Phase Synthesized near 250 GPa, Phys. Rev. Lett. **122**, 066001 (2019).

[4] C. Mailhiot, L. H. Yang, and A. K. McMahan, Polymeric nitrogen, Phys. Rev. B **46**, 14419 (1992).

[5] M. I. Eremets, A. G. Gavriliuk, I. A. Trojan, D. A. Dzivenko, and R. Boehler, Single-bonded cubic form of nitrogen, Nat. Mater. **3**, 558 (2004).

[6] C. Ji, A. A. Adeleke, L. Yang, B. Wan, H. Gou, Y. Yao, B. Li, Y. Meng, J. S. Smith, V. B. Prakapenka, W. Liu, G. Shen, W. L. Mao, and H.-k. Mao, Nitrogen in black phosphorus structure, Sci. Adv. **6**, eaba9206 (2020).

[7] D. Laniel, B. Winkler, T. Fedotenko, A. Pakhomova, S. Chariton, V. Milman, V. Prakapenka, L. Dubrovinsky, and N. Dubrovinskaia, High-pressure polymeric nitrogen allotrope with the black phosphorus structure, Phys. Rev. Lett. **124**, 216001 (2020).

[8] N. W. Ashcroft, Metallic hydrogen: A high-temperature superconductor?, Phys. Rev. Lett. **21**, 1748 (1968).

[9] K. Trachenko, B. Monserrat, C. J. Pickard, and V. V. Brazhkin, Speed of sound from fundamental physical constants, Sci. Adv. **6**, eabc8662 (2020).

[10] X. Ling, H. Wang, S. Huang, F. Xia, and M. S. Dresselhaus, The renaissance of black phosphorus, Proc. Natl. Acad. Sci. U.S.A. **112**, 4523 (2015).

[11] F. Xia, H. Wang, J. C. M. Hwang, A. H. C. Neto, and L. Yang, Black phosphorus and its isoelectronic materials, Nat. Rev. Phys. **1**, 306 (2019).

[12] Y. Xu, Z. Shi, X. Shi, K. Zhang, and H. Zhang, Recent progress in black phosphorus and black-phosphorus-analogue materials: properties, synthesis and applications, Nanoscale **11**, 14491 (2019).

[13] M. van Schilfgaarde, T. Kotani, and S. Faleev, Quasiparticle Self-Consistent GW Theory, Phys. Rev. Lett. **96**, 226402 (2006).

[14] D. Pashov, S. Acharya, W. R. Lambrecht, J. Jackson, K. D. Belashchenko, A. Chantis, F. Jamet, and M. van Schilfgaarde, Questaal: A package of electronic structure methods based on the linear muffin-tin orbital technique, Comput. Phys. Commun. **249**, 107065 (2020).

[15] B. Cunningham, M. Grüning, P. Azarhoosh, D. Pashov, and M. van Schilfgaarde, Effect of ladder diagrams on optical absorption spectra in a quasiparticle self-consistent
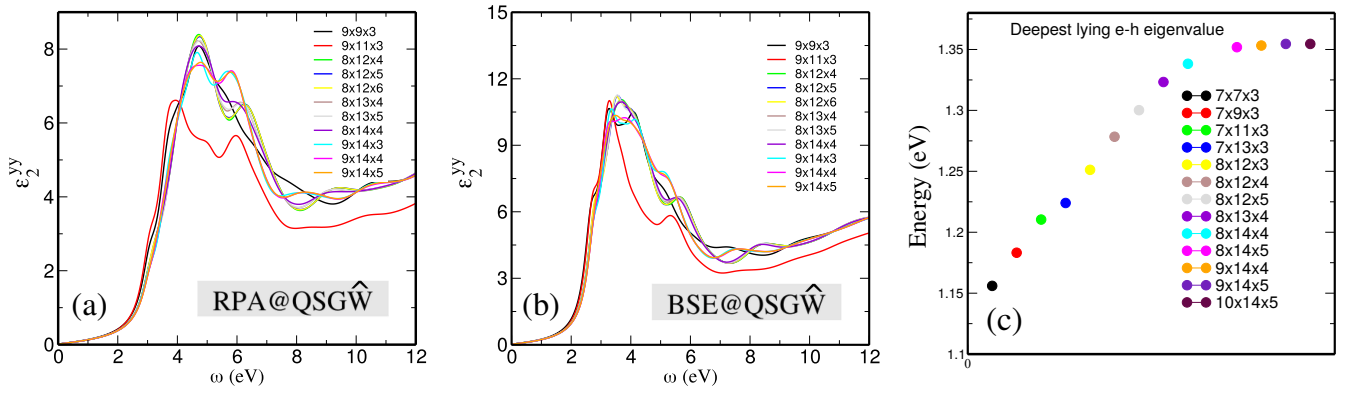
FIG. 9. (a),(b) The convergence of the RPA@QS$G\widehat{W}$ and BSE@QS$G\widehat{W}$ dielectric function $\varepsilon_2^{yy}(\omega)$ in bN with respect to the **k**-point mesh. (c) The convergence of the deepest lying dark e-h eigenvalue.

GW framework, Phys. Rev. Mater. **2**, 034603 (2018).

[16] B. Cunningham, M. Gruening, D. Pashov, and M. van Schilfgaarde, QSGW: Quasiparticle Self consistent *GW* with ladder diagrams in W (2021), arXiv:2106.05759 [cond-mat.mtrl-sci].

[17] I. Tamm, Relativistic Interaction of Elementary Particles, J. Phys. USSR **9**, 449 (1945).

[18] S. M. Dancoff, Non-adiabatic meson theory of nuclear forces, Phys. Rev. **78**, 382 (1950).

[19] G. Kresse and J. Furthmller, Efficiency of ab-initio total energy calculations for metals and semiconductors using a plane-wave basis set, Comp. Mat. Sci. **6**, 1550 (1996).

[20] G. Kresse and J. Furthmüller, Efficient iterative schemes for *ab initio* total-energy calculations using a plane-wave basis set, Phys. Rev. B **54**, 11169 (1996).

[21] M. Shishkin and G. Kresse, Implementation and performance of the frequency-dependent *GW* method within the PAW framework, Phys. Rev. B **74**, 035101 (2006).

[22] M. Shishkin and G. Kresse, Self-consistent *GW* calculations for semiconductors and insulators, Phys. Rev. B **75**, 235102 (2007).

[23] M. Kaltak, Merging GW with DMFT, PhD Thesis, University of Vienna, 2015, 231 pp.

[24] P. E. Blöchl, Projector augmented-wave method, Phys. Rev. B **50**, 17953 (1994).

[25] G. Kresse and D. Joubert, From ultrasoft pseudopotentials to the projector augmented-wave method, Phys. Rev. B **59**, 1758 (1999).

[26] J. P. Perdew, K. Burke, and M. Ernzerhof, Generalized Gradient Approximation Made Simple, Phys. Rev. Lett. **77**, 3865 (1996).

[27] N. Marzari and D. Vanderbilt, Maximally localized generalized Wannier functions for composite energy bands, Phys. Rev. B **56**, 12847 (1997).

[28] N. Marzari, A. A. Mostofi, J. R. Yates, I. Souza, and D. Vanderbilt, Maximally localized Wannier functions: Theory and applications, Rev. Mod. Phys. **84**, 1419 (2012).

[29] A. A. Mostofi, J. R. Yates, Y.-S. Lee, I. Souza, D. Vanderbilt, and N. Marzari, wannier90: A tool for obtaining maximally-localised Wannier functions, Comp. Phys. Commun. **178**, 685 (2008).

[30] T. Miyake and F. Aryasetiawan, Screened coulomb interaction in the maximally localized wannier basis, Phys. Rev. B **77**, 085122 (2008).

[31] A. Togo and I. Tanaka, First principles phonon calculations in materials science, Scr. Mater. **108**, 1 (2015).

[32] B. A. DeAngelis, R. E. Newnham, and W. B. White, Factor group analysis of the vibrational spectra of crystals: a review and consolidation, Am. Mineral. **57**, 255 (1972).

[33] T. C. T. Ting, On Anisotropic Elastic Materials for which Young's Modulus $E(n)$ is Independent of n or the Shear Modulus $G(n, m)$ is Independent of n and m, J. Elast. **81**, 271 (2006).

[34] S. E. Boulfelfel, G. Seifert, Y. Grin, and S. Leoni, Squeezing lone pairs: The $A17$ to $A7$ pressure-induced phase transition in black phosphorus, Phys. Rev. B **85**, 014110 (2012).

[35] D. Scelta, A. Baldassarre, M. Serrano-Ruiz, K. Dziubek, A. B. Cairns, M. Peruzzini, R. Bini, and M. Ceppatelli, Interlayer bond formation in black phosphorus at high pressure, Angew. Chem. Int. Ed. **56**, 14135 (2017).

[36] J. Klimeš, D. R. Bowler, and A. Michaelides, Van der waals density functionals applied to solids, Phys. Rev. B **83**, 195131 (2011).

[37] A. N. Rudenko, S. Yuan, and M. I. Katsnelson, Toward a realistic description of multilayer black phosphorus: From *GW* approximation to large-scale tight-binding simulations, Phys. Rev. B **92**, 085419 (2015).

[38] R. W. Keyes, The electrical properties of black phosphorus, Phys. Rev. **92**, 580 (1953).

[39] B. Kiraly, N. Hauptmann, A. N. Rudenko, M. I. Katsnelson, and A. A. Khajetoorians, Probing single vacancies in black phosphorus at the atomic level, Nano Lett. **17**, 3607 (2017).

[40] E. Carré, L. Sponza, A. Lusson, I. Stenger, E. Gaufrès, A. Loiseau, and J. Barjon, Excitons in bulk black phosphorus evidenced by photoluminescence at low temperature, 2D Mater. **8**, 021001 (2021).

[41] V. Tran, R. Soklaski, Y. Liang, and L. Yang, Layer-controlled band gap and anisotropic excitons in few-layer black phosphorus, Phys. Rev. B **89**, 235319 (2014).

[42] S. Acharya, D. Pashov, A. N. Rudenko, M. Rsner, M. van Schilfgaarde, and M. I. Katsnelson, Excitons in bulk and layered chromium tri-halides: From frenkel to the wannier-mott limit (2021), arXiv:2110.08174 [cond-mat.mtrl-sci].

[43] S. Appalakondaiah, G. Vaitheeswaran, S. Lebégue, N. E. Christensen, and A. Svane, Effect of van der Waals interactions on the structural and elastic properties of black phosphorus, Phys. Rev. B **86**, 035105 (2012).

[44] H. B. Ribeiro, M. A. Pimenta, and C. J. de Matos, Raman spectroscopy in black phosphorus, J. Raman Spectrosc. **49**, 76 (2018).